

Influence of backside surface morphology on passivation and contact characteristics of TOPCON solar cells



Chunlin Guo ^{a,b}, Rui Jia ^{a,b,*}, Xing Li ^{a,b,*}, Xiaorang Tian ^{a,b,*}, Jiawang Chen ^{a,b}, Huayun Ge ^{a,b}, Huiwei Huang ^c, Ling Yuan ^c, Chun Xu ^c

^a Institute of Microelectronics of the Chinese Academy of Sciences, Beijing 100029, China

^b University of Chinese Academy of Sciences, Beijing 100029, China

^c Shufeng Photovoltaic Technology, Jiangsu, China

ARTICLE INFO

Keywords:

Tunnel oxide

Specific contact resistance

Passivation characteristics

Surface topography

Polishing

ABSTRACT

Compared with P-PERC cells, the rear tunnel oxide/n + polysilicon passivation contact structure in N-TOPCon cells makes the influence of rear surface morphology more significant. In this work, the effects of different chemical etching methods and weight loss on the surface topography and passivation characteristics and contact resistance of $\text{SiO}_x/\text{n} + \text{poly Si}$ passivated contact structures were investigated by finely controlling the etching process. Studies have shown that for textured surfaces, both increasing the roundness of the pyramids (acid polishing) and flattening the pyramids (alkaline polishing) lead to a more uniform SiO_x layer, which improves surface passivation. The significant deterioration of the contact resistance of the alkali-polished flat surface may be more due to the influence of the thickness of the tunnel oxide layer and the concentration of trailing P doping in the substrate. Acid polishing preserves the round pyramid structure but removes the sharp pyramid tips, improving contact passivation while ensuring good metal contact. It can better balance the contradiction between passivation characteristics ($J_0 \sim 4.73\text{fA}/\text{cm}^2$, $J_{0,\text{metal}} \sim 67.26\text{fA}/\text{cm}^2$, $i\text{Voc} \sim 740 \text{ mV}$) and contact characteristics ($\rho_c, B \sim 1.67\text{m}\Omega\text{cm}^2$), and achieve the highest average cell efficiency (24.05%).

1. Introduction

At present, the efficiency of P-type PERC cells exceeds 23%, which is close to its efficiency limit, so the process of improving efficiency is slowing down [27,50]. Based on the concept of carrier selectivity, the German Institute ISFH analyzed the theoretical limit efficiencies of PERC, HIT, and TOPCon cells of 24.5%, 27.5%, and 28.7%, respectively [39]. Among them, the n-type TOPCon cell is widely considered to be one of the most promising next-generation high-efficiency crystalline silicon cell technologies after the PERC cell and has been extensively studied in recent years [8,9,10,11,29,230,31,35,45]. The efficiency of small-area double-sided metal contact N-type TOPCON solar cells prepared in the laboratory is as high as 25.8% [36]. The POLO-IBC with an interdigitated back contact structure combined with a passivation contact structure achieved an ultrahigh efficiency of 26.1% [17]. BJ-FBC uses back-junction full-area passivation contacts on the basis of double-sided metal contacts, which have also been proven to achieve > 26% efficiency [37]. In recent years, the efficiency of large-area Topcon

solar cells used for mass production has also continued to break through, with the highest reported efficiency reaching 25.7% [5,14].

The N-TOPCON solar cell structure is to prepare an ultra-thin tunnel oxide layer and a thin n + highly doped polysilicon layer on the back of the cell to form a passivation contact structure together [19,20,24,26,32,41,43,46,48,51]. Compared with the smooth surface silicon wafers used in the laboratory, it is difficult to form high-quality passivation contact structures on large-area rough surface silicon wafers used in solar cell industrial production. The reason for this is that the passivation quality is sensitive to the thickness of the SiO_x layer [21,22,23]. The increased roughness of the pyramidal $\text{Si}(111)$ surface leads to more surface defects than the polished $\text{Si}(111)$ surface, which in turn may affect the growth of the SiO_x layer [33]. The pyramidal morphology of pyramidal tips, faces, edges, and valleys contributes to the SiO_x inhomogeneity [3]. This causes the SiO_x layer near the pyramid valleys to become thinner than the pyramid tips or end faces, which can significantly affect the passivation performance [47]. At the same time, the low-reflectivity pyramidal surface allows more light into the

* Corresponding authors at: Institute of Microelectronics of the Chinese Academy of Sciences, Beijing 100029, China.

E-mail addresses: imesolar@126.com (R. Jia), lixing2021@ime.ac.cn (X. Li), tianxiaorang@ime.ac.cn (X. Tian).

polysilicon than the high-reflectivity surface, resulting in greater NIR parasitic losses (free carrier absorption) in n + polysilicon [13,40,42,44]. Therefore, under the requirements of improving passivation characteristics and optical absorption, a smoother and higher reflectivity polished surface is an effective optimization direction. However, metal contact points need to be optimized in the opposite direction. Pyramid faces are more conducive to forming good contacts, thereby reducing contact resistance and increasing FF. On the one hand, surface topography can affect the formation of silver crystallites [4,18,34]. On the other hand, the rough surface is easier to realize the direct transport of carriers. Silver crystallites transport carriers in four ways, among which direct transport between silver crystallites and metal grid lines (without glass layer in between) is very important to achieve low contact resistance [14,15]. This transfer is easier to achieve on the tips of pyramidal surfaces and similar rough surfaces that are not easily covered by layers of glass.

In the industrial mass production of solar cells, edge isolation after diffusion is a very important process step. Using laser edge isolation is a solution, but is less used today [28]. Wet chemical etching is the more commonly used method, and during this process, the topography of the backside can also be modified simultaneously to match the backside tunnel oxide/polysilicon fabrication process and screen printed metal contacts. For N-type TOPCon cells, the excellent passivation performance, contact performance and minimal parasitic absorption of the back tunnel oxide/N + polysilicon layer are the keys to achieve high efficiency. All three are affected by the topography of the rear surface. Some etching-related research has been done and promoted the further improvement of solar cell efficiency. Inline process using HNO_3/HF solution or batch process using alkaline solution are the two main process routes [2,7]. Etching with HNO_3/HF solution can round the pyramids [53], thereby obtaining superior light absorption characteristics compared with flat surfaces, and at the same time obtaining better passivation characteristics than textured surfaces, thereby improving efficiency [14,15]. Etching with alkaline solution can eliminate the influence of sharp pyramid tips, but it is necessary to strictly control the polishing process to obtain an ideal pyramid base size to reduce the impact on ohmic contact [6]. In order to obtain higher efficiencies for industrially fabricated TOPCon solar cells, optimization of the backside topography is necessary. However, the differences in passivation characteristics and contact characteristics between different wet etching processes and different conditions of the same etching process have not been carefully studied. Relevant research is needed to provide technical support for the selection and optimization of wet process in actual mass production.

In this work, a large-area (274.15 cm²) N-type TOPCon solar cell was fabricated using a screen-printed silver paste method to achieve metal–semiconductor contact. Electron-selective passivation contacts are based on the thermal oxide growth of a tunnel oxide layer and LPCVD deposition of an intrinsic polysilicon layer, followed by doping and recrystallization by thermal diffusion of POCl_3 in an industrial-scale quartz tube furnace. Different chemical etching methods (acid polishing and alkali polishing) are used to achieve modification of the backside topography. By finely controlling the etching amount, the difference in surface morphology after different polishing weight reductions achieved by acid polishing and alkali polishing was studied. The effects of different surface topography on doping concentration, passivation characteristics of contact and non-contact regions, and contact resistance were investigated. Based on the requirements of edge isolation and removal of the back diffusion PN junction, the effects of different back topography on the performance of TOPCon cells were explored. The study showed that acid polishing improved the surface flatness by rounding the pyramids while ensuring good metal contact, achieving a compromise between metal contact characteristics and passivation characteristics, and finally achieved the highest average solar cell efficiency of 24.05%. Compared with alkali polishing and alkali texturing samples, it increased by 0.33% and 0.18% respectively.

2. Experiment

A sample with a two-sided symmetric structure (shown in Fig. 1a) was used to investigate the properties of the tunnel oxide/phosphorous-doped polysilicon passivation contact structure. The substrate is an n-type commercial DWS mc-Si wafer ($166 \times 166 \text{ mm}^2$) with a thickness of $165 \pm 10 \mu\text{m}$ and a resistivity of $0.5\text{--}2 \Omega\cdot\text{cm}$. The preparation process is shown in Fig. 2(a). After texturing, the wafers were etched using two different chemical cleaning processes, as shown in Table 1, including (1) acid polishing and (2) alkali polishing. The additives used in this paper were all prepared by our laboratory. Through formula optimization and improvement, texturing additives can obtain uniform pyramid size and low reflectivity, and polishing additives can obtain good polishing properties and oxide layer protection.

Then, an ultra-thin tunnel oxide layer is grown using thermal oxidation, followed by the deposition of an intrinsic polysilicon layer by LPCVD [52]. Low-pressure phosphorous diffusion doping was performed using a tubular diffusion furnace. Use HF solution to remove PSG and perform Radio Corporation of America (RCA) cleaning. Finally, double-sided silicon nitride films are grown by PECVD. The dopant profiles of the samples were measured by an ECV device (WEP CVP21). J_0 , Auger in the c-Si substrate was estimated using simulations on EDNA2 provided by PVlighthouse. Minority carrier lifetime (τ_{eff}), Implied open circuit voltage ($i\text{Voc}$), and recombination current (J_0) were tested by WCT-120 Sinton(@5E15) [25], which can show the passivation characteristics of the symmetric samples. To evaluate the difference in passivation of metal contacts with different surface topographies, J_0 , metal was tested. For the symmetrical sample shown in Fig. 1(a), four different metallization fractions (0.02, 0.04, 0.06, 0.08) were screen printed and fired, then the metal was removed using HNO_3/HCl solution. Test the J_0 of symmetrical samples with different metallization area fractions, and perform simple linear interpolation of the test data points using the method proposed by Fellmeth et al [12]. Scanning electron microscopy (SEM, Hitachi, S4800) was used to characterize the surface and cross-sectional morphologies after different wet etching. Use a reflectance tester to determine the reflectance. The contact resistance of the metal grid lines of the samples with different morphologies was tested by the transfer-length-method (TLM, GP-4 TEST) to evaluate whether the samples formed good metal contact with the silver paste [16]. Samples of both structures were tested to evaluate the contact resistance under different current transfer modes. The first structure is shown in Fig. 3(a), that is, the backside structure of a standard TOPCON solar cell. Due to the thin thickness of the tunnel oxide layer and the existence of pinholes in the oxide layer, there may be localized metal burn-through. At the same time, the doping tailing of P atoms in the substrate is also inevitable, so the transport path of the current includes the transport through the polysilicon and the substrate. The second structure is shown in Fig. 3(b), the polysilicon region is separated by a thick oxide layer insulating region ($>100 \text{ nm}$), and the current only flows through the polysilicon region. The sheet resistance of this sample after phosphorous diffusion is $40\text{--}45 \Omega/\text{sq}$. The test results are called back contact resistivity ($\rho_{c,B}$) and polysilicon contact resistivity ($\rho_{c,P}$).

The structure of the TOPCon solar cell is shown in Fig. 1(b), and its process flow is shown in Fig. 2(b). After texturing in an alkaline solution, the front emitter was formed by low-pressure BCl_3 diffusion in an industrial-scale quartz tube furnace. Then, the backside and edge diffusion junctions are removed by wet chemical cleaning etch, and the topography of the backside is modified. In order to keep the front surface pyramids unaffected during the backside chemical etching process, an inline process single-side etching method (SSE) was adopted and BSG was used as a protective film. The specific process is shown in Table 1. Thermal oxidation grows a tunnel oxide layer. 80 nm intrinsic polysilicon is grown in LPCVD followed by POCl_3 diffusion with a sheet resistance of $30\text{--}35 \Omega/\text{sq}$. After etching the Wrap-around polysilicon, $\text{Al}_2\text{O}_3/\text{SiNx}$ (ALD/PECVD) and SiNx (PECVD) stacks were deposited on the front and back sides, respectively. The thickness of SiNx is $80\text{--}90 \text{ nm}$

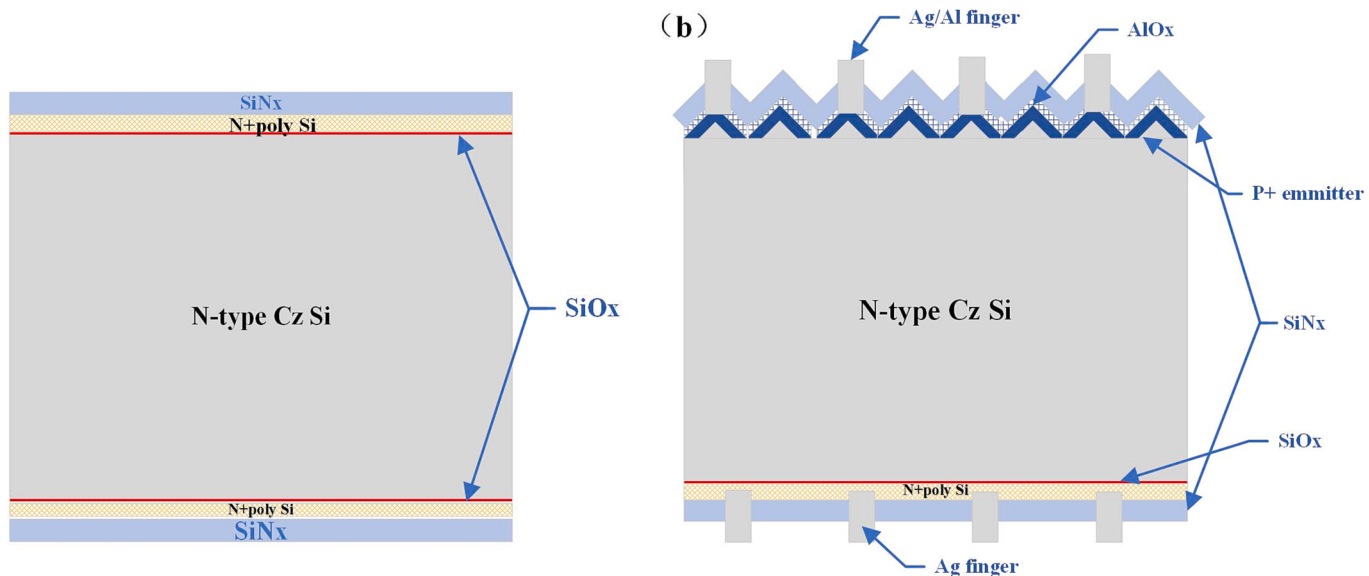


Fig. 1. (a)Schematic diagram of the double-sided symmetric sample (b)Schematic diagram of TOPCON solar cell sample.

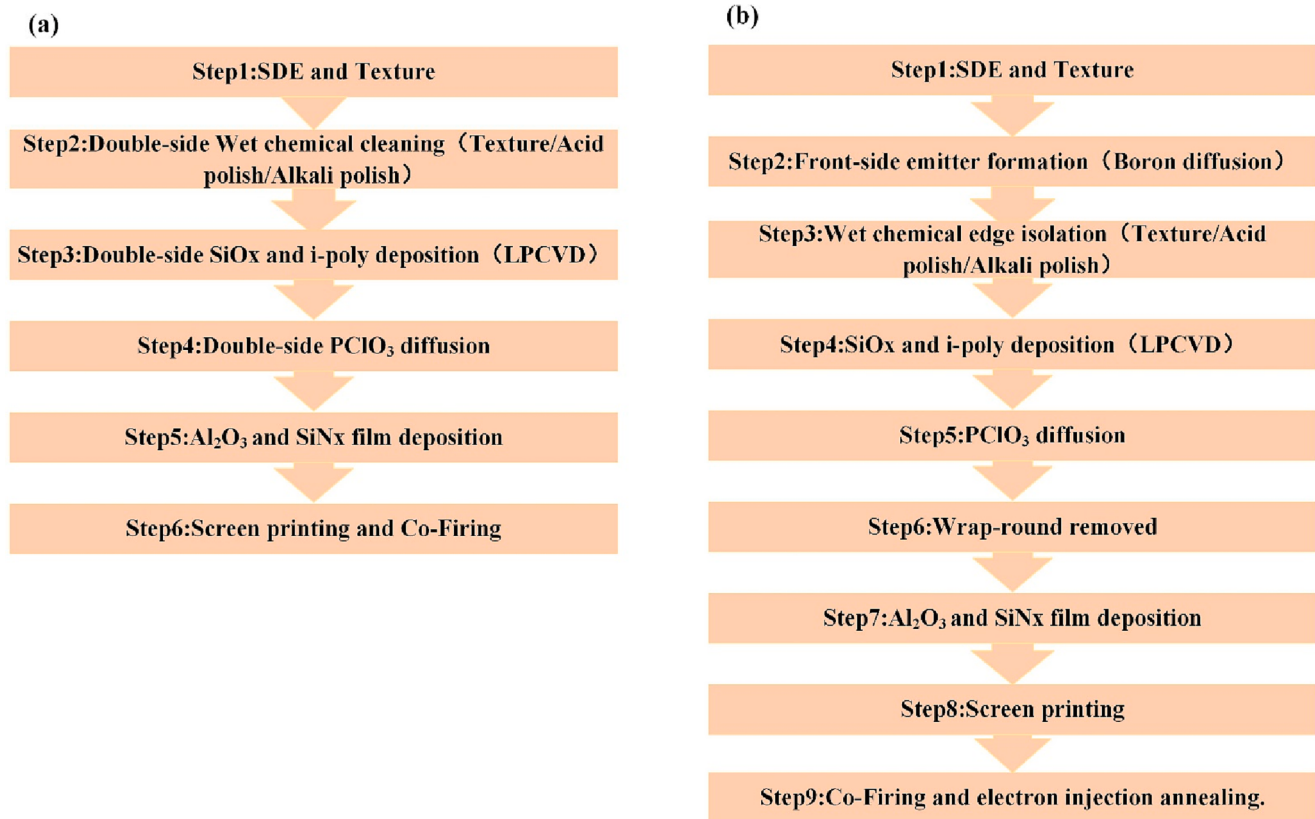


Fig. 2. (a)Preparation process of double-sided symmetric sample. (b)Preparation process of TOPCON solar cell sample (LPCVD ex-situ doping).

and the refractive index is 2.05–2.1. Finally, metal contact is achieved by screen printing followed by co-fired annealing. Activation of H passivation is achieved by electron injection annealing. The photoelectric conversion efficiency is determined by measuring the current–voltage (I-V) characteristic curve. External quantum efficiency (EQE), internal quantum efficiency (IQE), and light reflection were measured using the PVE300-IVT. The optical loss analysis results are from the Current Loss Analysis Calculator V1.4 Optical Loss provided by the Solar Energy Research Institute of Singapore [49].

3. Results and discussion

3.1. Influence of surface morphology on passivation and contact characteristics of SiO_x/n + poly Si structures

According to the weight loss of polishing, the experimental samples were divided into 4 groups, and the weight loss of silicon wafers was 0.1 g–0.4 g respectively. The textured sample is referred to as T0. For alkali-polished groups, they are referred to as P1, P2, P3, and P4 in

Table 1

Three etching processes for the preparation of double-sided symmetrical structure samples and solar cells.

| | | Process I | Process II | Process III |
|------------------|--|--|-----------------------------------|---------------------------------|
| Texture | double-sided symmetric sample solar cell | Texture-double side | / | / |
| | | | HF-single side | Texture 2-single side |
| Acid polishing | double-sided symmetric sample solar cell | Acid polishing-double side HF-single side | / | Acid polishing-single side / |
| Alkali polishing | double-sided symmetric sample solar cell | Alkali polishing-double side HF-single side | Alkali polishing-single side / | Alkali polishing-single side |

Note:

Texture -double side:the volume ratio of KOH: Si surface texture additive1:H₂O = 2:1:280 at 75–80°C in the batch-type process.

HF-single side: the volume ratio of HF = 10–12% at room temperature in the inline process.

Acid polishing-single/double side: the volume ratio of HF:HNO₃:H₂O = 2:7:13 at room temperature in the inline process.

Alkali polishing-single/double side: the volume ratio of KOH: Si surface Polishing Additive:H₂O = 4:5:16 at 65–75 °C in the batch-type process.

Texture 2-single side:the volume ratio of KOH: Si surface texture additive2:H₂O = 3:1:220 at 80–82°C in the batch-type process.

sequence according to the increase in weight loss. For acid-polished groups, they are called E1, E2, E3, and E4. Fig. 4 is the SEM photographs of the surface morphology after different wet chemical treatments (texture (a), acid polishing (b-e), alkali polishing (f-i)).

The complete pyramid can be seen in the textured sample. The original textured sample T0 had a reflectance of 10.3%. The weight loss of acid-polished samples is controlled mainly by changing the belt speed of the chain etching cleaner and changing the ratio of chemical solutions. The weight loss of alkali-polished samples is mainly controlled by changing the chemical reaction time. Fig. 5(a) shows the alkali polishing weight loss as a function of time, indicating that no reaction occurred during the first 40 s due to the presence of the surface oxide layer. After polishing for 40 s, a violent reaction begins accompanied by smoothing

of the surface and weight loss. After polishing for 90 s, the weight loss reaches 0.1 g, 170 s reaches 0.2 g, 285 s reaches 0.3 g, and 460 s reaches 0.4 g. The polishing speed is first fast and then slow. The test points are fitted to a curve, as shown by the red dotted line in Fig. 5(a). Under the polishing conditions set in this experiment, the silicon wafer weight loss and polishing time satisfy the following equation:

$$y = -0.0463 + 0.00168x - (1.58E - 6)x^2 \quad (1)$$

It can be seen that both acid polishing and alkali polishing can significantly change the surface roughness of silicon wafers, but the surface roughness of acid-polished samples is significantly lower than that of alkali-polished samples. After acid polishing, the shape of the pyramid of the sample has changed, and the sharp pyramid tip disappears and becomes a sloped hill, similar to a rounded pyramid. As the weight reduction increases, the slope becomes smaller, the sharpness of the peak decreases, and the flatness of the surface increases. With the increase in weight loss, the reflectance of acid-polished samples was 30.5%, 32.9%, 35%, and 36%, respectively. For alkali polishing samples, the tip of the pyramid is completely flattened, and only the square base of the pyramid can be seen. As the weight loss increases, the size of the square increases. From the scanning electron microscope images, it can be seen that the square sizes are 6 μm, 13 μm, 19 μm, and 27 μm, respectively. The increase in the base square symbolizes the increase in flatness. Even if the sample weight is only reduced by 0.1 g (P1), a relatively flat surface can already be obtained, but local protrusions are retained. As shown in Fig. 5(b), corresponding to different weight loss, the reflectance of alkali-polished samples is 39.68%, 43.51%, 44.49%, and 45.38%.

The effect of different surface topography on the passivation quality of TOPCon is shown in Fig. 6. It can be observed that both alkali polishing and acid polishing can improve the passivation characteristics of symmetrical samples. Compared with acid polishing, alkali polishing makes the surface smoother, and the quality and uniformity of the ultra-thin tunnel oxide layer are better, so the passivation characteristics are more advantageous [21,22,23]. The passivation characteristics become better as the etch weight loss increases. Among them, the passivation quality of the alkali polished sample is the best, the reverse saturation current J₀ of the P4 sample is the smallest (3.23fA/cm²), the minority carrier lifetime is the longest (2579 μs), and the iVoc is the largest (742.7 mV). The passivation quality of the alkali textured sample T0 is the worst, the reverse saturation current J₀ is the largest (5.93fA/cm²), the minority carrier lifetime is the smallest (1663 μs), and the iVoc is also the smallest (735 mV). The passivation quality of the acid-polished samples was intermediate between the other two. However, acid

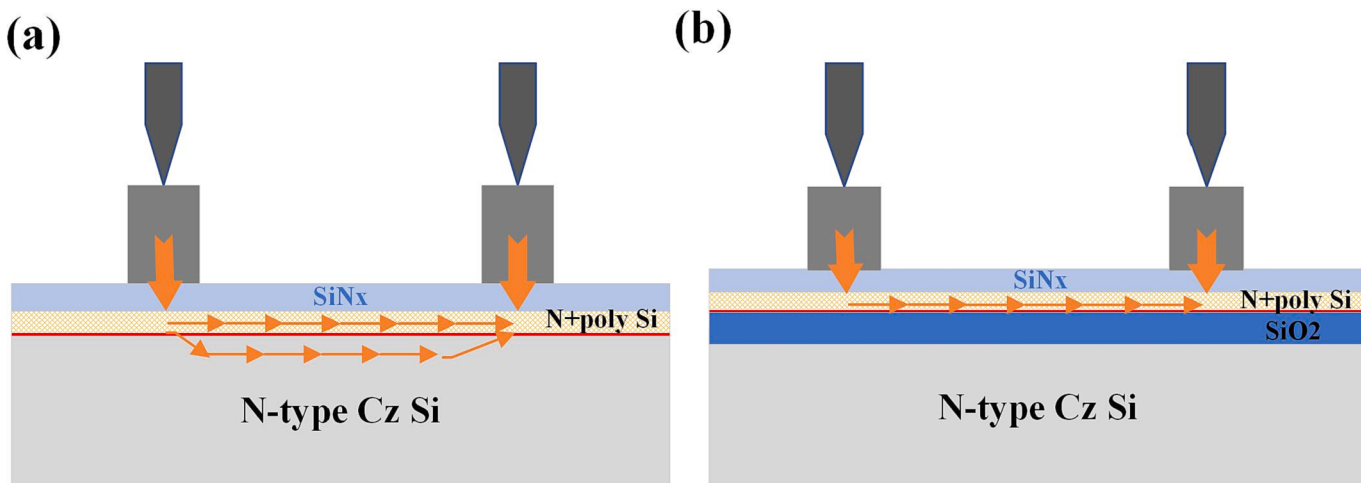


Fig. 3. (a) Schematic diagram of TOPCON solar cell back contact resistance(ρ_c , b) test structure. (b) Schematic diagram of TOPCON solar cell n + polysilicon contact resistance test structure($\rho_{c,p}$).

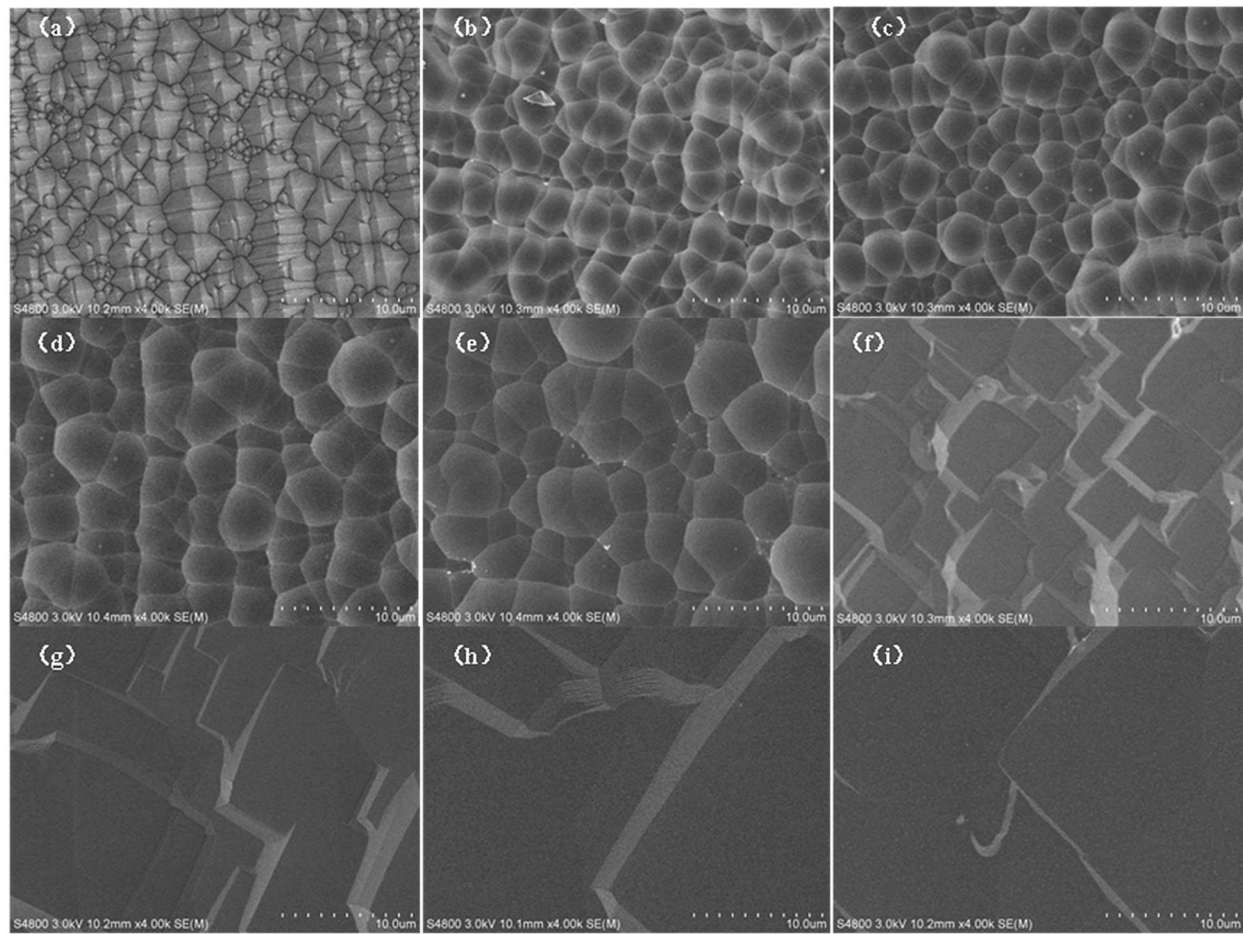


Fig. 4. SEM images of the surface morphologies after different backside wet chemical treatments (texture (a), acid polishing (b-e), alkali polishing (f-i)).

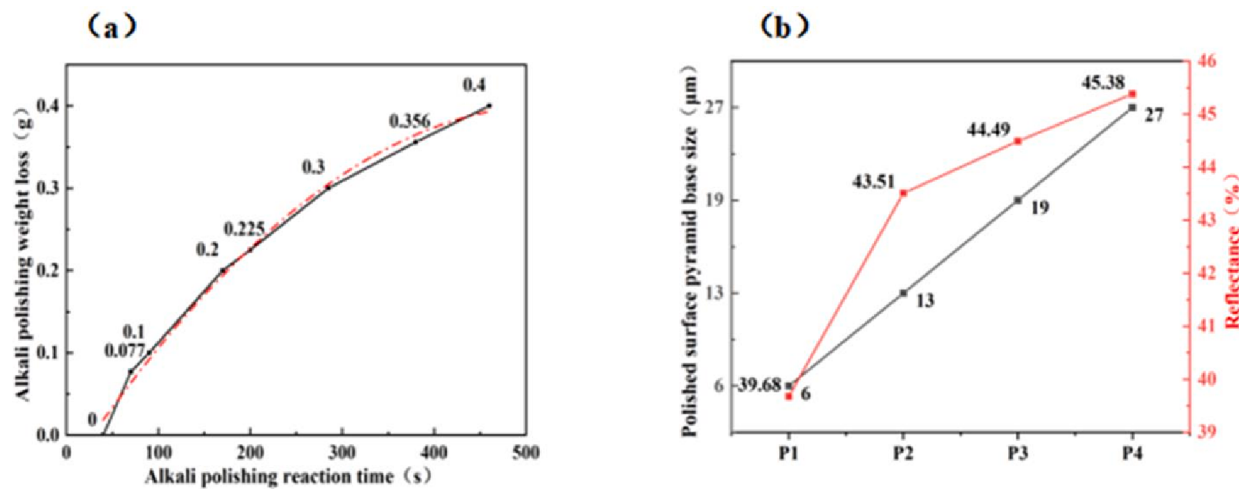


Fig. 5. (a) Alkali polishing weight loss as a function of reaction time (the red dotted line is a polynomial fitting curve) (b)Pyramid base size and reflectance under different alkali polishing conditions. (For interpretation of the references to colour in this figure legend, the reader is referred to the web version of this article.)

polishing and alkali polishing both increase iV_{oc} significantly. In the case of the same weight loss, the iV_{oc} of alkali polishing is 2 mV higher than that of acid polishing. In the case of weight loss of 0.4 g, the iV_{oc} of E4 and P4 samples reaches the maximum, which are 740 mV and 742.7 mV, respectively. It can also be seen that although the acid-polished sample does not achieve a smooth and flat surface, the removal of the high pyramid tip can significantly and effectively improve the

passivation characteristics of the tunnel oxide polysilicon structure.

Fig. 6(c) shows the phosphorus doping concentrations of the samples with different backside morphologies after $POCl_3$ diffusion. For the doping concentration in polysilicon, there is a difference between the samples with different surface topography, which is caused by the difference in surface area. For the doping concentration in c-Si, it can be shown that the barrier effect of the tunneling oxide layer on diffusion in

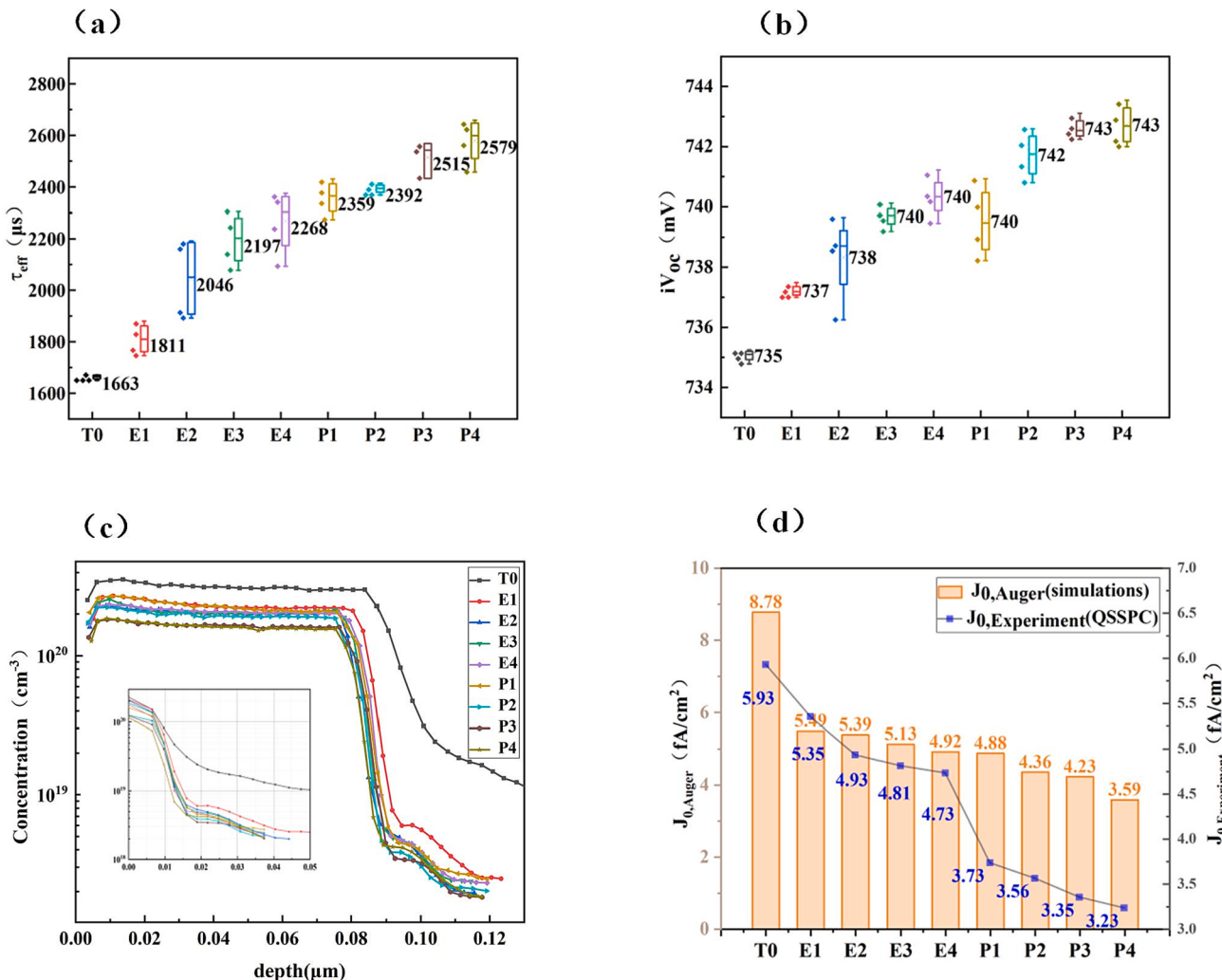


Fig. 6. (a) τ_{eff} , (b) iV_{oc} of samples with different morphologies. (c) Active dopant concentration obtained from ECV measurements. (d) J_0, Auger from EDNA2 simulation and J_0 from QSSPC.

samples with different surface topography, which can partly explain the differences in the quality and passivation performance of the tunneling oxide layer in samples with different topography. The P tailing doping concentration in single crystal silicon is specially extracted, as shown in Fig. 6(c), where depth = 0 is the tunnel oxide layer/single crystal silicon interface. Inside the c-Si substrate, due to the blocking effect of the oxide layer on the diffusion of P atoms, the doping concentration of the acid-polished and alkali-polished samples will drop rapidly to below $1E19\text{cm}^{-3}$ in the range of 20 nm. It can be observed that the doping concentration of the alkali-polished samples is always lower than that of the acid-polished samples. This may simply be due to surface area differences. Whereas in the textured samples, at the tunneling oxide/silicon substrate interface, the doping concentration of phosphorus atoms does not drop rapidly to a lower level like in other samples but starts to decrease slowly from a higher concentration ($1E20\text{cm}^{-3}$). This shows that the diffusion barrier effect of the tunneling oxide layer of the alkali textured sample is poor, and the excessive diffusion of phosphorus atoms into the silicon substrate will intensify the Auger recombination in the substrate and weaken the passivation effect. This is due to the fact that the pyramidal structure of the textured sample leads to inconsistent thicknesses of the tunneling oxide layer at different positions of the pyramid, resulting in the cracking of the thinner oxide layer in some areas during high-temperature annealing. Typically, the SiO_x thickness at the top, edges, and faces of the pyramids is thicker than that near the pyramid valleys. Since the passivation properties from n + polysilicon/

SiO_x contacts are dependent on the thickness of SiO_x, the increased roundness of the pyramids (acid polishing) and flattening of the pyramids (alkaline polishing) may result in a more uniform SiO_x layer and thus improved surface passivation.

For high-quality silicon, when the impurity concentration exceeds $1E18\text{cm}^{-3}$ and the surface passivation has been done well enough, Auger recombination will become the main recombination mechanism at high injection levels. The doping concentration of the material will significantly affect the Auger recombination. For the P-doping concentration distribution in Fig. 6(c), we tried to use EDNA2 to simulate to estimate J_0, Auger in the c-Si substrate, and the results are shown in Fig. 6(d). By properly setting the simulation parameters, the relative value of J_0, Auger can be obtained, as shown in Fig. 6(d). In the textured samples, J_0, Auger is the largest, reaching 8.78fA/cm^2 . The alkali-polished P4 group reaches a minimum of 3.23fA/cm^2 . Simulation J_0, Auger results show the same variation trend as test J_0 results, but the simulation results are too large. This is similar to findings in other studies [31]. It could be due to overestimation of J_0, Auger within EDNA2 (e.g. due to small errors in BGN or other models in the software, or simply overestimation errors in dopant distribution within silicon) or underestimation of J_0 . In fact, the difference in J_0 is the combined effect of Auger recombination J_0, Auger , SiO_x/c-Si chemical passivation, and other factors.

The difference in J_0 caused by different surface topography does not seem to be large, but it is known that the main purpose and advantage of

the passivation contact structure is to reduce the degradation caused by the metal contact. But even so, high temperature annealing still causes some damage to the passivation contact structure, thus causing more recombination in the metal contact area. In this regard, the $J_{0,\text{metal}}$ of silver paste screen-printed and annealed samples with different morphologies were tested to characterize the difference in metal contact passivation with different surface morphologies. The results are shown in Fig. 7. Different surface topography has a huge impact on $J_{0,\text{metal}}$, and the effect is more significant than that of J_0 . For the textured sample, its $J_{0,\text{metal}}$ is the largest, reaching 131.6fA/cm^2 , which may be related to the formation of more silver crystallites due to the existence of the pyramid tip. Both acid polishing and alkali polishing can significantly reduce $J_{0,\text{metal}}$, but under the same polishing weight loss, the $J_{0,\text{metal}}$ of acid polishing samples is always greater than that of alkali polishing samples. The likely reasons are that the flat surface allows for thicker film thickness and better densification, and the lower actual annealing temperature due to high reflectivity results in less metal burn-through. More importantly, surface planarization seriously affects the formation of silver crystallites. Although the acid-polished samples retained the rounded pyramids, $J_{0,\text{metal}}$ was significantly reduced with increasing polishing weight loss, suggesting that the removal of sharp pyramid apexes and reduction of texture slopes can also improve metal contact passivation properties. The E4 and P4 samples with the largest weight loss achieved the largest $J_{0,\text{metal}}$, which were 51.46 and 41.77fA/cm^2 , respectively. This is almost a third of the $J_{0,\text{metal}}$ of the texturing sample. This indicates that the adjustment of the surface topography has a much greater effect on the passivation performance of the metal contact area than that of the non-metal contact area.

On the other hand, we need to consider the contact between samples with different morphologies and the silver paste. Fig. 8 shows the contact resistivity of samples with different surface topography. The two structures described in Fig. 3 were tested respectively, and the test results were $\rho_{c,B}$ and $\rho_{c,P}$. It can be seen from Fig. 6(1) that, $\rho_{c,B}$ (texturing sample) < $\rho_{c,B}$ (acid polishing sample) ≪ $\rho_{c,B}$ (alkali polishing sample). The $\rho_{c,B}$ of the texturing sample is the smallest, reaching $0.69\text{m}\Omega\cdot\text{cm}^2$. With the increase of polishing weight loss, the surface of the sample becomes flatter, and the contact resistivity $\rho_{c,B}$ increases. It can be seen that with the increase in weight loss, the increase of $\rho_{c,B}$ of the alkali-polished samples is much larger than that of the acid-polished samples. It can be observed from Fig. 6(2) that for $\rho_{c,P}$, the difference between samples with different morphologies is not as large as $\rho_{c,B}$. The texturing sample also obtained the smallest $\rho_{c,P}$, but its value was much larger than $\rho_{c,B}$, which was $5.46\text{m}\Omega\cdot\text{cm}^2$. With the increase of polishing weight loss, the contact resistivity $\rho_{c,P}$ increased slightly. At the same time, the difference between the acid-polished and

alkali-polished samples was very small. When the weight loss of the sample increases to 0.3 g , the $\rho_{c,P}$ of the acid-polished and alkali-polished samples are very similar.

We observed that for samples with the same morphology, the difference between $\rho_{c,B}$ and $\rho_{c,P}$ was very large, and showed different trends after wet chemical etching. The difference in the measured values of the two sample structures may be due to the different current transport paths. $\rho_{c,B}$ is affected by the contact between metal-polysilicon and the contact between metal-polysilicon-tunnel oxide-single-crystal silicon substrate. $\rho_{c,P}$ is only affected by the metal/polysilicon contact. This is because the thick oxide layer blocks the transport of current through the substrate, which only occurs in polysilicon. The small differences in $\rho_{c,P}$ in samples with different morphologies may indicate that the polysilicon and metal in the three morphological samples have formed similar and good ohmic contacts. Minor differences may come from the metal-covered surface area, and actual firing temperature [18,44]. After the polishing weight loss is relatively large, the change of the surface area also slows down, which may also be the reason why $\rho_{c,P}$ does not continue to increase. Since $\rho_{c,P}$ shows a smaller increase with polishing weight loss, the change in $\rho_{c,B}$ is more likely to be related to the smoother surface after polishing and the reduction of pinholes in the tunnel oxide layer. Theoretically, the silver paste does not burn through the tunnel oxide layer. But in fact, samples with different morphologies may have different pinhole densities due to the presence of stress during the high-temperature diffusion process, and these pinholes may become areas where the metal burns through. More pinholes are formed on the surface of the pyramid while flattening the surface topography reduces the density of pinholes. For the region of metal burn-through, the P doping concentration in the sample substrates with different morphologies may have a significant effect on the metal contact. As shown in Fig. 6(c), the difference in doping concentration in the substrates with different morphologies and the test results of contact resistance are consistent with each other.

Additionally, in the transport path of electrons between silicon and metal, the current flowing directly through the silver crystallites to the silver grid lines is the most influential transport mode. These direct contacts are mainly concentrated at the tips of the silicon pyramids, as there is no glass covering in this area [34]. The presence of pyramid tips in the textured structure increases direct transport and thus reduces contact resistivity. With the increase of acid polishing weight loss, the tip of the pyramid is gradually rounded, the uncovered area of the glass layer is gradually reduced, the existence of this transmission mode is reduced, and the contact resistivity is gradually increased. While alkali polishing directly flattens the tip of the pyramid, direct transmission is almost non-existent. In addition, thicker silicon nitride films deposited by PECVD due to planarized surfaces may also result in a reduction in the number of silver crystallites incorporated into the silicon. At the same time, the increased reflectivity of the polished topography slightly reduces the actual temperature during the high-temperature fast co-firing process, which may affect the formation of deep silver crystallites.

Therefore, we believe that when metal firing is performed on the TOPCon structure, it is inevitable that the oxide layer is burnt through by the metal. This has a significant effect on the contact resistance $\rho_{c,B}$ and is very dependent on the surface topography. In the practical fabrication of TOPCon cells, it may be necessary to have backside roughness to improve metal contact, even at the expense of passivation.

3.2. Effect of back surface topography on TOPCon solar cell efficiency

In the TOPCon solar cell fabrication process, edge isolation and backside morphology modification after B diffusion are usually performed simultaneously. This requires that a good surface topography must be achieved based on the complete removal of the edge and backside B-diffusion PN junctions to achieve high parallel resistance, superior passivation characteristics, and Good contact characteristics with metal. Under the condition that the weight reduction meets the

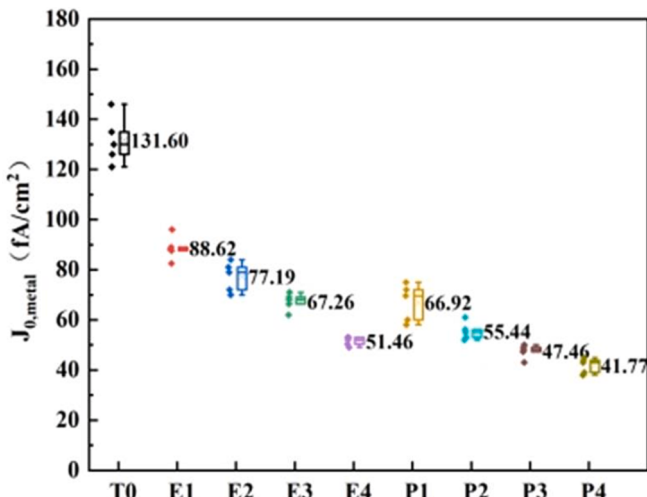
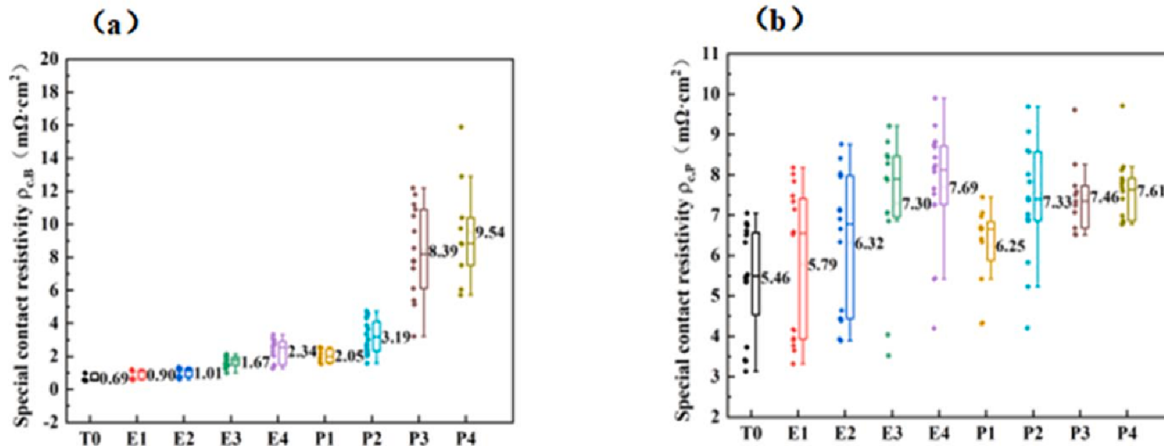


Fig. 7. $J_{0,\text{metal}}$ of alkali polished, acid polished, and textured samples.

Fig. 8. Contact resistivity (a) $\rho_{c,B}$ (b) $\rho_{c,P}$ of different morphologies.

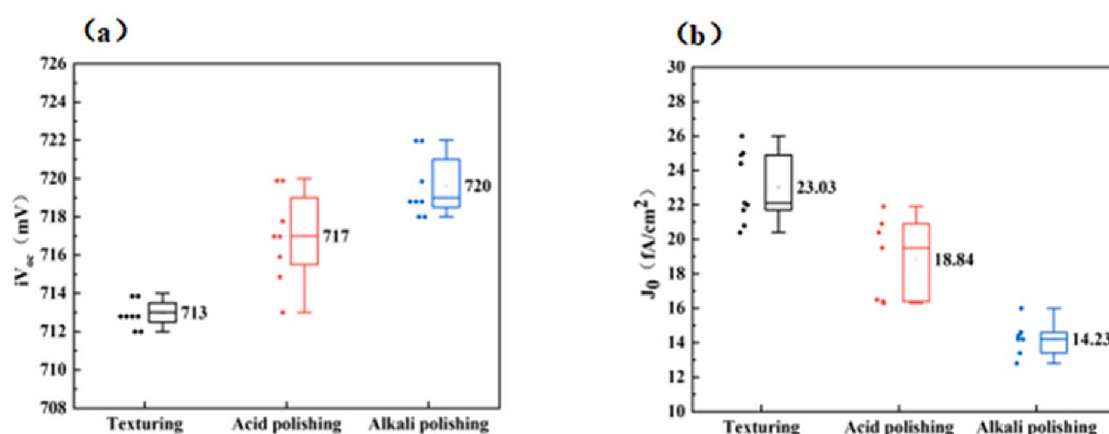
edge isolation requirement (0.3 g), the TOPCon solar cell precursor samples J0 and iVoc we prepared are shown in Fig. 9. We can see that the iVoc of the alkali texturing, acid polishing, and alkali polishing samples are 713 mV, 717 mV, 720 mV, and J0 are 23.03, 18.84, and 14.23 fA/cm², which corresponds well with the test data of the double-sided symmetrical sample. J0 seems to show a larger difference compared to the double-sided symmetrical structure sample, which may be due to the background doping concentration of the back structure of the solar cell and the influence of other process preparation processes. This shows that in terms of the passivation characteristics of solar cell precursors before printing metal contact, alkali polishing is better than acid etching and alkali texturing. From the electrical properties of the battery shown in Table 2, due to poor metal contact, alkali polishing has a large series resistance and a very low fill factor (80.86%), even if its opening voltage (710 mV) and current (41.32 mA/cm²) are improved, but the final battery efficiency (23.72%) drops significantly. The open voltage (701 mV) and short-circuit current(40.77 mA/cm²) of the alkali texturing sample are the lowest, but its fill factor (83.52%) has a greater advantage and the efficiency(23.87%) is in the middle. The open voltage (706 mV), short-circuit current(41.05 mA/cm²), and FF(82.99%) of the acid-polished sample are all in the middle, and the final efficiency (24.05%) is the highest. This indicates that for the currently used silver paste, the acid-polished surface can better balance the contradiction between the metal contact and surface passivation, and obtain higher conversion efficiency. But for the alkali-polished samples, the significant deterioration of the metal contact causes serious losses, which are difficult to make up for the increase in open voltage and short-circuit current brought about by the flat surface. It is difficult to obtain high

Table 2
I-V parameters of Texture, Acid polishing, Alkali polishing, TOPCon cells.

| | Uoc (mV) | Jsc (mA/ cm ²) | Rs (mΩ) | FF (%) | Eff (%) |
|----------------------------|---------------|--------------------------------|--------------|-------------|--------------|
| Texturing sample | 701 | 40.77 | 3.23 | 83.52 | 23.87 |
| Acid polishing sample | 706 | 41.05 | 3.49 | 82.99 | 24.05 |
| Alkali polishing sample | 710 | 41.32 | 7.23 | 80.86 | 23.72 |

efficiency due to poor passivation characteristics and the large current loss of alkali-textured samples. We also observed that compared with the iVoc of the precursor sample, the Voc of TOPCon solar cells decreased by 12 mV(Texturing sample), 11 mV(Acid polishing sample), and 10 mV (Alkali polishing sample), respectively. This reveals the difference in the electrical performance of solar cells with different morphologies due to the degradation introduced by metal recombination [42].

The influencing factors of short-circuit current are complex. The different carrier recombination of samples with different surface topography may be an important influencing factor. At the same time, there may also be differences in the metal contacts of samples with different morphologies, which may affect the carrier transport. Through the quantum efficiency test, we can simply analyze the loss mechanism of the short-circuit current. It can be observed from Fig. 10(a) that the differences in EQE and reflectivity brought about by different back surface topography are more reflected in the 900–1100 nm long-wavelength light [1,38]. This is because long-wavelength light needs

Fig. 9. (a)iVoc and (b)J₀ of the precursor structure samples.

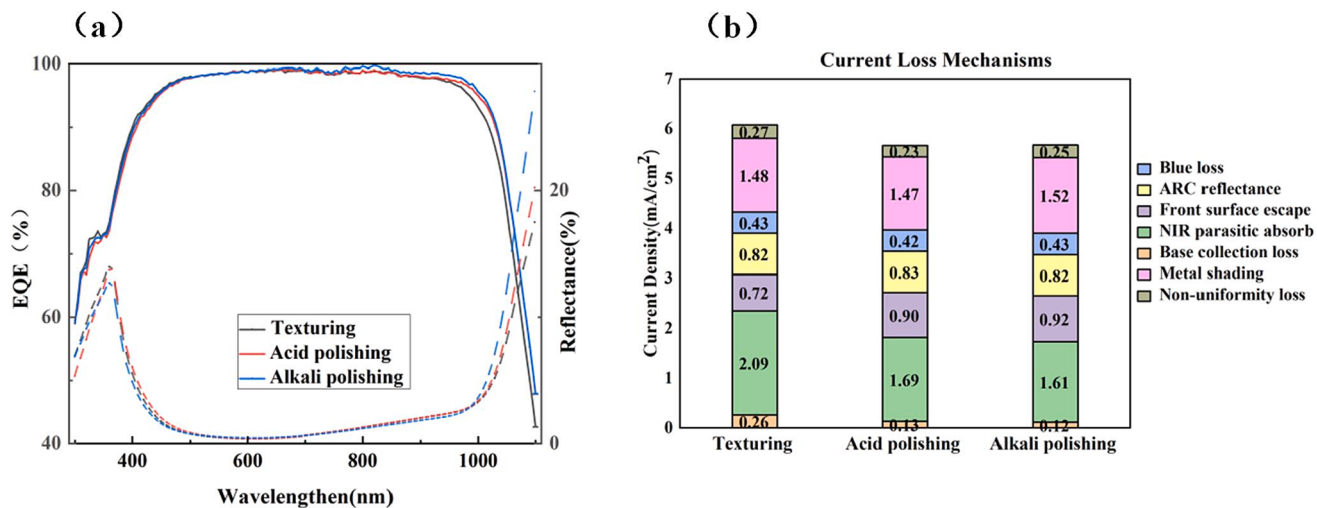


Fig. 10. (a) EQE of three morphological solar cell samples (b) Current loss Mechanisms analysis of solar cell samples with three morphologies.

to travel deeper into the silicon to be absorbed. When long-wavelength light is incident on the backside of the silicon substrate, the difference in the topography of the backside leads to a significant difference in the optical path. The low reflectivity of the textured sample allows more light to enter the heavily doped polysilicon, while the high reflectivity of the acid-polished and alkali-polished samples allows more incident light to be reflected into the substrate. This ultimately leads to a difference in near-infrared optical absorption, manifested as a decrease in EQE with increasing backside surface roughness. A more intuitive result can be seen from the analysis of the current loss mechanism in Fig. 10(b). The parasitic loss of the alkali-textured sample has a large absorption in the near-infrared band because the rough surface allows more long-wavelength light to enter the heavily doped polysilicon, resulting in greater free carrier absorption. The flat surface of the alkali-polished sample makes the long-wavelength light reflect back to the substrate and be absorbed again, thereby increasing the short-circuit current, but at the same time causing the front surface escape loss to increase. Acid-polished samples are also effective in reducing near-infrared parasitic absorption loss, but slightly worse than alkali-polished samples. Other optical losses are mainly related to metal shading, front surface blue light absorption, and ARC reflection. This is a problem that needs to be solved in future research. The optimization of the front selective emitter, metal grid lines, and anti-reflection film will further promote the improvement of solar cell efficiency.

The above studies show that three different chemical etching methods can produce significant differences in post-diffusion edge isolation. Flatter surface topography, fewer surface defects, and dangling bonds can greatly improve the open-circuit voltage of solar cells. At the same time, it can also improve the reflection of long-wavelength light on the back surface to improve the absorption and reduce its entry into the heavily doped polysilicon to be recombined. A flatter surface will also cause a significant increase in the contact resistance on the backside of the solar cell, which will manifest as a huge difference in FF. Compared to the alkali-textured and alkali-polished samples, the acid-polished samples eliminated pyramidal spikes to achieve better passivation characteristics, while the roughened surface achieved better metal contact. Therefore, the contradiction between passivation and contact is better balanced, and the highest efficiency can be achieved.

4. Conclusion

In summary, by finely controlling the etching process, the effects of different chemical etching methods and weight loss on the surface

morphology, tunnel oxide/n + polysilicon passivation characteristics, and contact resistance were studied. Studies have shown that for textured surfaces, increasing the roundness of the pyramids (acid polishing) and flattening the pyramids (alkaline polishing) both lead to a more uniform SiO_x layer, which improves the passivation contact. With the increase of polishing weight loss, the passivation contact characteristics gradually improved (the metal contact J_0 , metal changes more significantly), and the contact characteristics gradually deteriorated. Under the same weight loss, the passivation performance of the acid-polished sample is always slightly worse than that of the alkali-polished sample, and its contact resistance is significantly better than that of the alkali-polished sample. The flat surface formed by alkali polishing caused severe contact resistance deterioration, which does not seem to be caused by the poor contact between the metal paste and polysilicon, but is more likely to be caused by the thickness of the tunnel oxide layer and the tailing doping concentration in the substrate. Alkali-polished samples can significantly improve the passivation effect and light absorption, but the significant reduction of FF makes the efficiency low. In this work, the acid polishing process can effectively achieve edge isolation, balance passivation ($J_0 \sim 4.73\text{fA}/\text{cm}^2$, J_0 , metal $\sim 67.26\text{fA}/\text{cm}^2$, $i\text{Voc} \sim 740\text{ mV}$), and contact characteristics ($\rho_c, B \sim 1.67\text{m}\Omega \cdot \text{cm}^2$), the best average cell efficiency (24.05%) was achieved. Future research on matching surface topography with silver paste will facilitate further efficiency improvements.

Declaration of Competing Interest

The authors declare that they have no known competing financial interests or personal relationships that could have appeared to influence the work reported in this paper.

Acknowledgements

This work was supported by the National Key Research and Development Program of China (2020YFB1506503, 2022YFF0709500, 2018YFB1500200), National Natural Science Foundation of China (NSFC, Grant Nos. 12035020, 52072399, 62074165, 12175305, 62104253 and 12105357), Natural Science Foundation of Beijing Municipality (4192064, 1212015).

References

- [1] Baker-Finch, S.C., McIntosh, K.R., Yan, D., Fong, K.C., Kho, T.C., 2014. Near-infrared free carrier absorption in heavily doped silicon. *J. Appl. Phys.* 116 (6) <https://doi.org/10.1063/1.4893176>.

- [2] Belhadj Mohamed, S., Ben Rabha, M., Bessais, B., 2013. Porous silicon/NaOH texturization surface treatment of crystalline silicon for solar cells. *Sol. Energy* 94, 277–282. <https://doi.org/10.1016/j.solener.2013.04.026>.
- [3] Chandra Mandal, N., Biswas, S., Acharya, S., Panda, T., Sadhukhan, S., Sharma, J. R., Nandi, A., Bose, S., Kole, A., Das, G., Maity, S., Chaudhuri, P., Saha, H., 2020. Study of the properties of SiO_x layers prepared by different techniques for rear side passivation in TOPCon solar cells. *Mater. Sci. Semicond. Process.* 119 <https://doi.org/10.1016/j.mssp.2020.105163>.
- [4] Chaudhary, A., Hoß, J., Lossen, J., Huster, F., Kopecek, R., van Swaaij, R., Zeman, M., 2022. Influence of Silicon Substrate Surface Finish on the Screen-Printed Silver Metallization of Polysilicon-Based Passivating Contacts. *physica status solidi (a)* 219 (9). <https://doi.org/10.1002/pssa.202100869>.
- [5] Chen, D., Chen, Y., Wang, Z., Gong, J., Liu, C., Zou, Y., He, Y., Wang, Y., Yuan, L., Lin, W., Xia, R., Yin, L., Zhang, X., Xu, G., Yang, Y., Shen, H., Feng, Z., Altermatt, P. P., Verlinden, P.J., 2020. 24.58% total area efficiency of screen-printed, large area industrial silicon solar cells with the tunnel oxide passivated contacts (i-TOPCon) design. *Sol. Energy Mater. Sol. Cells* 206. <https://doi.org/10.1016/j.solmat.2019.110258>.
- [6] Chen, W., Yu, Y., Wang, W., Chen, P., Ke, Y., Liu, W., Wan, Y., 2022. Influence of rear surface pyramid base microstructure on industrial n-TOPCon solar cell performances. *Sol. Energy* 247, 24–31. <https://doi.org/10.1016/j.solener.2022.10.017>.
- [7] Cornagliotti, E., Ngamo, M., Tous, L., Russell, R., Horzel, J., Hendrickx, D., Douhard, B., Prajapati, V., Janssens, T., Poortmans, J., 2012. Integration of Inline Single-side Wet Emitter Etch in PERC Cell Manufacturing. *Energy Procedia* 27, 624–630. <https://doi.org/10.1016/j.egypro.2012.07.120>.
- [8] Feldmann, F., Bivour, M., Reichel, C., Hermle, M., Glunz, S.W., 2014. Passivated rear contacts for high-efficiency n-type Si solar cells providing high interface passivation quality and excellent transport characteristics. *Sol. Energy Mater. Sol. Cells* 120, 270–274. <https://doi.org/10.1016/j.solmat.2013.09.017>.
- [9] Feldmann, F., Bivour, M., Reichel, C., Steinkemper, H., Hermle, M., Glunz, S.W., 2014. Tunnel oxide passivated contacts as an alternative to partial rear contacts. *Sol. Energy Mater. Sol. Cells* 131, 46–50. <https://doi.org/10.1016/j.solmat.2014.06.015>.
- [10] Feldmann, F., Simon, M., Bivour, M., Reichel, C., Hermle, M., Glunz, S.W., 2014. Efficient carrier-selective p- and n-contacts for Si solar cells. *Sol. Energy Mater. Sol. Cells* 131, 100–104. <https://doi.org/10.1016/j.solmat.2014.05.039>.
- [11] Fell, A., 2013. A Free and Fast Three-Dimensional/Two-Dimensional Solar Cell Simulator Featuring Conductive Boundary and Quasi-Neutrality Approximations. *IEEE Trans. Electron Devices* 60 (2), 733–738. <https://doi.org/10.1109/ted.2012.2231415>.
- [12] Fellmeth, T., Born, A., Kimmerle, A., Clement, F., Biro, D., Preu, R., 2011. Recombination at Metal-Emitter Interfaces of Front Contact Technologies for Highly Efficient Silicon Solar Cells. *Energy Procedia* 8, 115–121. <https://doi.org/10.1016/j.egypro.2011.06.111>.
- [13] Firat, M., Payo, M.R., Duerinckx, F., Luchies, J.-M., Lenes, M., Poortmans, J., 2019. Characterization of absorption losses in rear side n-type polycrystalline silicon passivating contacts, 15th International Conference on Concentrator Photovoltaic Systems (CPV-15).
- [14] Firat, M., Sivaramakrishnan Radhakrishnan, H., Payo, M.R., Choulat, P., Badran, H., van der Heide, A., Govaerts, J., Duerinckx, F., Tous, L., Hajjiah, A., Poortmans, J., 2022. Large-area bifacial n-TOPCon solar cells with in situ phosphorus-doped LPCVD poly-Si passivating contacts. *Sol. Energy Mater. Sol. Cells* 236. <https://doi.org/10.1016/j.solmat.2021.111544>.
- [15] Firat, M., Sivaramakrishnan Radhakrishnan, H., Recamán Payo, M., Duerinckx, F., Tous, L., Poortmans, J., 2022. In situ phosphorus-doped polycrystalline silicon films by low pressure chemical vapor deposition for contact passivation of silicon solar cells. *Sol. Energy* 231, 78–87. <https://doi.org/10.1016/j.solener.2021.11.045>.
- [16] Guo, S., Gregory, G., Gabor, A.M., Schoenfeld, W.V., Davis, K.O., 2017. Detailed investigation of TLM contact resistance measurements on crystalline silicon solar cells. *Sol. Energy* 151, 163–172. <https://doi.org/10.1016/j.solener.2017.05.015>.
- [17] Haase, F., Hollemann, C., Schäfer, S., Merkle, A., Rienäcker, M., Krügener, J., Brendel, R., Peibst, R., 2018. Laser contact openings for local poly-Si-metal contacts enabling 26.1%-efficient POLO-IBC solar cells. *Sol. Energy Mater. Sol. Cells* 186, 184–193. <https://doi.org/10.1016/j.solmat.2018.06.020>.
- [18] Han, H., Choi, D., Jeong, S., Kang, D., Park, H., Bae, S., Kang, Y., Lee, H.-S., Kim, D., 2021. Effects of surface morphology on Ag crystallite formation in screen-printed multi-crystalline Si solar cells. *Mater. Sci. Semicond. Process.* 128 <https://doi.org/10.1016/j.mssp.2021.105759>.
- [19] Herrmann, D., Fell, A., Lohmüller, S., Mikolasch, G., Schmiga, C., Wolf, A., Glunz, S.W., 2021. Microstructure beneath screen-printed silver contacts and its correlation to metallization-induced recombination parameters. *Sol. Energy Mater. Sol. Cells* 230. <https://doi.org/10.1016/j.solmat.2021.111182>.
- [20] Herrmann, D., Lohmüller, S., Hoffler, H., Fell, A., Brand, A.A., Wolf, A., 2019. Numerical Simulations of Photoluminescence for the Precise Determination of Emitter Contact Recombination Parameters. *IEEE J. Photovoltaics* 9 (6), 1759–1767. <https://doi.org/10.1109/jphotov.2019.2938400>.
- [21] Kale, A.S., Nemeth, W., Guthrey, H., Kennedy, E., Norman, A.G., Page, M., Al-Jassim, M., Young, D.L., Agarwal, S., Stradins, P., 2019. Understanding the charge transport mechanisms through ultrathin SiO_x layers in passivated contacts for high-efficiency silicon solar cells. *Appl. Phys. Lett.* 114 (8) <https://doi.org/10.1063/1.5081832>.
- [22] Kale, A.S., Nemeth, W., Guthrey, H., Nanayakkara, S.U., LaSalvia, V., Theingi, S., Findley, D., Page, M., Al-Jassim, M., Young, D.L., Stradins, P., Agarwal, S., 2019. Effect of Crystallographic Orientation and Nanoscale Surface Morphology on Poly-Si/SiO_x Contacts for Silicon Solar Cells. *ACS Appl. Mater. Interfaces* 11 (45), 42021–42031. <https://doi.org/10.1021/acsami.9b11889>.
- [23] Kale, A.S., Nemeth, W., Guthrey, H., Page, M., Al-Jassim, M., Young, D.L., Agarwal, S., Stradins, P., 2019. Modifications of Textured Silicon Surface Morphology and Its Effect on Poly-Si/SiO_x Contact Passivation for Silicon Solar Cells. *IEEE J. Photovoltaics* 9 (6), 1513–1521. <https://doi.org/10.1109/jphotov.2019.2937230>.
- [24] Kruse, C.N., Schafer, S., Haase, F., Mertens, V., Schulte-Huxel, H., Lim, B., Min, B., Dullweber, T., Peibst, R., Brendel, R., 2021. Simulation-based roadmap for the integration of poly-silicon on oxide contacts into screen-printed crystalline silicon solar cells. *Sci Rep* 11 (1), 996. <https://doi.org/10.1038/s41598-020-79591-6>.
- [25] Liu, B., Chen, Y., Yang, Y., Chen, D., Feng, Z., Altermatt, P.P., Verlinden, P., Shen, H., 2016. Improved evaluation of saturation currents and bulk lifetime in industrial Si solar cells by the quasi steady state photoconductance decay method. *Sol. Energy Mater. Sol. Cells* 149, 258–265. <https://doi.org/10.1016/j.solmat.2016.01.032>.
- [26] Liu, Z., Yang, Z., Wang, W., Yang, Q., Han, Q., Ma, D., Cheng, H., Lin, Y., Zheng, J., Liu, W., Liao, M., Chen, H., Wang, Y., Zeng, Y., Yan, B., Ye, J., 2021. Numerical and experimental exploration towards a 26% efficiency rear-junction n-type silicon solar cell with front local-area and rear full-area polysilicon passivated contacts. *Sol. Energy* 221, 1–9. <https://doi.org/10.1016/j.solener.2021.04.020>.
- [27] Melskens, J., van de Loo, B.W.H., Macco, B., Black, L.E., Smit, S., Kessels, W.M.M., 2018. Passivating Contacts for Crystalline Silicon Solar Cells: From Concepts and Materials to Prospects. *IEEE J. Photovoltaics* 8 (2), 373–388. <https://doi.org/10.1109/jphotov.2018.2797106>.
- [28] Otaegi, A., Fano, V., Rasool, M.A., Gutierrez, J.R., Jimeno, J.C., Azkona, N., Cereceda, E., 2017. Progress in the explanation and modeling of the laser-induced damage of edge-isolation processes in crystalline silicon solar cells. *Sol. Energy* 155, 847–853. <https://doi.org/10.1016/j.solener.2017.07.030>.
- [29] Padhamnath, P., Buatis, J.K., Khanna, A., Nampalli, N., Nandakumar, N., Shanmugam, V., Aberle, A.G., Duttagupta, S., 2020. Characterization of screen printed and fire-through contacts on LPCVD based passivating contacts in monoPoly™ solar cells. *Sol. Energy* 202, 73–79. <https://doi.org/10.1016/j.solener.2020.03.087>.
- [30] Padhamnath, P., Nampalli, N., Khanna, A., Nagarajan, B., Aberle, A.G., Duttagupta, S., 2022. Progress with passivation and screen-printed metallization of Boron-doped monoPoly™ layers. *Sol. Energy* 231, 8–26. <https://doi.org/10.1016/j.solener.2021.11.015>.
- [31] Padhamnath, P., Nampalli, N., Nandakumar, N., Buatis, J.K., Naval, M.-J., Aberle, A.G., Duttagupta, S., 2020. Optoelectrical properties of high-performance low-pressure chemical vapor deposited phosphorus-doped polysilicon layers for passivating contact solar cells. *Thin Solid Films* 699. <https://doi.org/10.1016/j.tsf.2020.137886>.
- [32] Polzin, J.-I., Feldmann, F., Steinhauser, B., Hermle, M., Glunz, S., 2018. Realization of TOPCon using industrial scale PECVD equipment, AIP Conference Proceedings 2018.
- [33] Polzin, J.-I., Feldmann, F., Steinhauser, B., Hermle, M., Glunz, S.W., 2019. Study on the interfacial oxide in passivating contacts, 15th International Conference on Concentrator Photovoltaic Systems (CPV-15).
- [34] Pysch, D., Mette, A., Filipovic, A., Glunz, S.W., 2009. Comprehensive analysis of advanced solar cell contacts consisting of printed fine-line seed layers thickened by silver plating. *Prog. Photovolt. Res. Appl.* 17 (2), 101–114. <https://doi.org/10.1002/pip.855>.
- [35] Reusch, M., Bivour, M., Hermle, M., Glunz, S.W., 2013. Fill Factor Limitation of Silicon Heterojunction Solar Cells by Junction Recombination. *Energy Procedia* 38, 297–304. <https://doi.org/10.1016/j.egypro.2013.07.281>.
- [36] Richter, A., Benick, J., Feldmann, F., Fell, A., Hermle, M., Glunz, S.W., 2017. n-Type Si solar cells with passivating electron contact: Identifying sources for efficiency limitations by wafer thickness and resistivity variation. *Sol. Energy Mater. Sol. Cells* 173, 96–105. <https://doi.org/10.1016/j.solmat.2017.05.042>.
- [37] Richter, A., Müller, R., Benick, J., Feldmann, F., Steinhauser, B., Reichel, C., Fell, A., Bivour, M., Hermle, M., Glunz, S.W., 2021. Design rules for high-efficiency both-sides-contacted silicon solar cells with balanced charge carrier transport and recombination losses. *Nat. Energy* 6 (4), 429–438. <https://doi.org/10.1038/s41560-021-00805-w>.
- [38] Rudiger, M., Greulich, J., Richter, A., Hermle, M., 2013. Parameterization of Free Carrier Absorption in Highly Doped Silicon for Solar Cells. *IEEE Trans. Electron Devices* 60 (7), 2156–2163. <https://doi.org/10.1109/ted.2013.2262526>.
- [39] Schmidt, J., Peibst, R., Brendel, R., 2018. Surface passivation of crystalline silicon solar cells: Present and future. *Sol. Energy Mater. Sol. Cells* 187, 39–54. <https://doi.org/10.1016/j.solmat.2018.06.047>.
- [40] Sheng, J., Ma, Z., Cai, W., Ma, Z., Ding, J., Yuan, N., Zhang, C., 2019. Impact of phosphorus diffusion on n-type poly-Si based passivated contact silicon solar cells. *Sol. Energy Mater. Sol. Cells* 203. <https://doi.org/10.1016/j.solmat.2019.110120>.
- [41] Steinhauser, B., Jäger, U., Benick, J., Hermle, M., 2014. PassDop rear side passivation based on Al2O3/a-SiCx B stacks for p-type PERL solar cells. *Sol. Energy Mater. Sol. Cells* 131, 129–133. <https://doi.org/10.1016/j.solmat.2014.05.001>.
- [42] Stodolny, M.K., Lenes, M., Wu, Y., Janssen, G.J.M., Romijn, I.G., Luchies, J.R.M., Geerligs, L.J., 2016. n-Type polysilicon passivating contact for industrial bifacial n-type solar cells. *Sol. Energy Mater. Sol. Cells* 158, 24–28. <https://doi.org/10.1016/j.solmat.2016.06.034>.
- [43] Tao, K., Li, Q., Hou, C., Jiang, S., Wang, J., Jia, R., Sun, Y., Li, Y., Jin, Z., Liu, X., 2017. Application of a-Si/μc-Si hybrid layer in tunnel oxide passivated contact n-type silicon solar cells. *Sol. Energy* 144, 735–739. <https://doi.org/10.1016/j.solener.2017.01.061>.

- [44] Tsai, C.-Y., 2020. Parasitic photon process versus productive photon process: a theoretical study of free-carrier absorption in conventional and hot-carrier solar cells. *J. Phys. D Appl. Phys.* 53 (50) <https://doi.org/10.1088/1361-6463/abb1e6>.
- [45] Wang, Q., Wu, W., Chen, D., Yuan, L., Yang, S., Sun, Y., yang, S., Zhang, Q., Cao, Y., Qu, H., Yuan, N., Ding, J., 2020a. Study on the cleaning process of n+-poly-Si wraparound removal of TOPCon solar cells. *Solar Energy* 211, 324–335. <https://doi.org/10.1016/j.solener.2020.09.028>.
- [46] Wang, Q., Wu, W., Li, Y., Yuan, L., Yang, S., Sun, Y., Yang, S., Zhang, Q., Cao, Y., Qu, H., Yuan, N., Ding, J., 2021. Impact of boron doping on electrical performance and efficiency of n-TOPCon solar cell. *Sol. Energy* 227, 273–291. <https://doi.org/10.1016/j.solener.2021.08.075>.
- [47] Wang, Q., Wu, W., Yuan, N., Li, Y., Zhang, Y., Ding, J., 2020. Influence of SiO_x film thickness on electrical performance and efficiency of TOPCon solar cells. *Sol. Energy Mater. Sol. Cells* 208. <https://doi.org/10.1016/j.solmat.2020.110423>.
- [48] Wilking, S., Beckh, C., Ebert, S., Herguth, A., Hahn, G., 2014. Influence of bound hydrogen states on BO-regeneration kinetics and consequences for high-speed regeneration processes. *Sol. Energy Mater. Sol. Cells* 131, 2–8. <https://doi.org/10.1016/j.solmat.2014.06.027>.
- [49] Wong, J., Raj, S., Ho, J.W., Wang, J., Lin, J., 2016. Voltage Loss Analysis for Bifacial Silicon Solar Cells: Case for Two-Dimensional Large-Area Modeling. *IEEE J. Photovolt.* 6 (6), 1421–1426. <https://doi.org/10.1109/jphotov.2016.2598261>.
- [50] Yan, D., Cuevas, A., Phang, S.P., Wan, Y., Macdonald, D., 2018. 23% efficient p-type crystalline silicon solar cells with hole-selective passivating contacts based on physical vapor deposition of doped silicon films. *Appl. Phys. Lett.* 113 (6) <https://doi.org/10.1063/1.5037610>.
- [51] Zeng, Y., Tong, H., Quan, C., Cai, L., Yang, Z., Chen, K., Yuan, Z., Wu, C.-H., Yan, B., Gao, P., Ye, J., 2017. Theoretical exploration towards high-efficiency tunnel oxide passivated carrier-selective contacts (TOPCon) solar cells. *Sol. Energy* 155, 654–660. <https://doi.org/10.1016/j.solener.2017.07.014>.
- [52] Zhou, Y., Tao, K., Liu, A., Jia, R., Bao, J., Jiang, S., Sun, Y., Yang, S., Wang, Q., Zhang, Q., Yang, S., Cao, Y., Qu, H., 2020. Screen-printed n-type industry solar cells with tunnel oxide passivated contact doped by phosphorus diffusion. *Superlattice. Microst.* 148 <https://doi.org/10.1016/j.spmi.2020.106720>.
- [53] Zin, N., McIntosh, K., Kho, T., Franklin, E., Fong, K., Stocks, M., Wang, E.-C., Ratcliff, T., Blakers, A., 2016. Rounded Rear Pyramidal Texture for High Efficiency Silicon Solar Cells, 2016 IEEE 43rd Photovoltaic Specialists Conference (PVSC).